Bis(Vinylenedithio)-Tetrathiafulvalene-Based Coordination Networks

Federica Solano, Pascale Auban-Senzier, Iwona Olejniczak, Boleslaw Barszcz, Tomasz Runka, Pere Alemany, Enric Canadell, Narcis Avarvari, Nicolas Zigon

Bis(Vinylenedithio)-Tetrathiafulvalene-Based Coordination Networks

Federica Solano,[1] Pascale Auban-Senzier,[2] Iwona Olejniczak,[3] Bolesław Barszcz,[3] Tomasz Runka,[4] Pere Alemany,[5] Enric Canadell,*[,6] Narcis Avarvari,*[,1] Nicolas Zigon*[,1]

[1] F. Solano, Dr. N. Avarvari, Dr. N. Zigon, Univ Angers, CNRS, MOLTECH-ANJOU, SFR MATRIX, F-49000 Angers, France. E-mail: narcis.avarvari@univ-angers.fr; nicolas.zigon@univ-angers.fr

[2] Dr. P. Auban-Senzier, Université Paris-Saclay, CNRS, UMR 8502, Laboratoire de Physique des Solides, 91405 Orsay, France

[3] Dr. I. Olejniczak, Dr. B. Barszcz Institute of Molecular Physics, Polish Academy of Sciences, Smoluchowskiego 17, 60-179 Poznań, Poland

[4] Prof. T. Runka, Faculty of Materials Engineering and Technical Physics, Poznan University of Technology, Piotrowo 3, 60-965 Poznań, Poland

[5] Prof. P. Alemany, Departament de Ciència de Materials i Química Física and Institut de Química Teòrica i Computacional (IQTCUB), Universitat de Barcelona, Martí i Franquès 1, 08028 Barcelona, Spain

[6] Prof. E. Canadell, Institut de Ciència de Materials de Barcelona, ICMAB-CSIC, Campus de la UAB, E-08193 Bellaterra, Spain, and Chemistry Section, Royal Academy of Sciences and Arts of Barcelona, La Rambla 115, 08002 Barcelona, Spain, E-mail: canadell@icmab.es

ABSTRACT

Novel coordination polymers embedding electroactive moieties present a high interest in the development of porous conducting materials. While tetrathiafulvalene (TTF) based metal-organic frameworks were reported to yield through-space conducting frameworks, the use of S-enriched scaffolds remains elusive in this field. Herein is reported the employment of bis(vinylenedithio)-tetrathiafulvalene (BVDT-TTF) functionalized with pyridine coordinating moieties in coordination polymers. Its combination with various transition metals yielded four isostructural networks, whose conductivity increased upon chemical oxidation with iodine. The oxidation was confirmed in a single-crystal to single-crystal X-ray diffraction experiment for the Cd(II) complex. Raman spectroscopy measurements and DFT calculations confirmed the oxidation state of the bulk materials, and band structure calculations assessed the ground state as an electronically localized antiferromagnetic state, while the conduction occurs in a 2D manner. These results are shedding light to comprehend how to improve through-space conductivity thanks to sulfur enriched ligands.

INTRODUCTION

Porous conductive materials are appealing for a wide range of applications, in particular as battery or fuel cell electrodes or as supercapacitors.[1–3] In that area metal−organic frameworks (MOFs) span a tremendous enthusiasm thanks to their high versatility and various pore size availability. MOFs are crystalline porous materials constructed from metal ions or clusters and organic linkers whose properties are directed by the ligands and metal physical properties and spatial organization.[4,5] Thanks to their crystalline porous structures and to the various chemical compositions accessible, these materials are extremely beneficial to gas storage, controlled drug delivery, optical sensing, heterogeneous catalysis or water harvesting.[6–10] Typically, the vast majority of the networks are formed with organic ligands having a huge HOMO-LUMO gap and/or a poor orbital overlap with the inorganic part, precluding the formation of long-range electronic pathways. Consequently, MOFs usually show poor electrical conduction properties. Conductive MOFs are expected to yield applications in electrochemical sensing[11], thermoelectrics[12], fuel cells[2], and supercapacitors[13].

It is only lately that electroactive MOFs have emerged as a new class of promising materials, mixing porosity and conductivity. Several mechanisms are reported to bring conductivity in MOFs, such as through-bond, through-space, redox-hopping or guest promoted redox hopping.[14,15] In the “through-space” approach, π–π and orbital overlap between adjacent organic moieties creates a conduction band within the material. This is particularly true for ligands presenting a tendency to arrange themselves through π–π stacks. For example, compounds with a large π surface such as naphthalenediimide or triphenylene have been reported to yield conductive MOFs,[16–18] or even, recently, metallic ones.[19] In this regard, ligands scaffolds based on tetrathiafulvalenes (TTFs) have been used for a dozen of years in the structure of MOFs to improve their charge mobility and conductivity.[20,21] TTF-tetrabenzoate (TTFTB) represents a landmark in this field, while TTF-tetracarboxylic acid provided semiconducting nonporous solids.[22] Dincă *et al.* demonstrated the high charge mobility of the TTFTB-based networks, and the dependency of the electrical properties towards the cation diameter.[20,23] Using metal-dithiolene in the ligand scaffolds provides an alternative platform to the tetrathiafulvalene and leads to heterobimetallic conductive networks, whose integration in electrodes provided an efficient glucose sensor.[24,25]

Pyridine stands as another ubiquitous coordinating moiety for MOF synthesis. They have been also widely used to implement TTF as a redox active ligand in coordination chemistry.[26,27] The TTF-

tetrapyridyl ligand was extensively explored for MOFs synthesis and was combined with Fe^{II} to yield spin-crossover materials.[28] The vast coordination chemistry of the pyridyl ligand afforded networks with various topologies,[29] where a strong influence of the counterion was noted.[30] The expansion of the TTF scaffold to a flexible tetrathiopyridyl-TTF provided polymers whose structural properties depended on the conformation adopted by the ligand.[31] Alternative design with an ethylenedithio-capped TTF-bis(thiopyridyl) supplied 1-D coordination polymers where the redox active cores overlapped in an interdigitated fashion, thus enhancing the conduction properties.[32]

Tetrathiafulvalene (TTF) and its derivatives have been widely investigated for their impressive electron-donating abilities and for their reversible oxidation to the radical cation ($TTF^{+\bullet}$) and dication (TTF^{2+}) forms.[33–35] The possibility of obtaining an open-shell within a MOF structure paves the way towards highly conductive materials. Moreover, extended scaffolds such as bis(ethylenedithio)tetrathiafulvalene (BEDT-TTF) contain four extra sulphur atoms and saturated non planar CH_2CH_2 group, thus favouring the formation of S···S multiple side intermolecular interaction in the layers of the radical cations to generate superconducting states at low temperatures for BEDT-TTF based organic conductors.[34,36]

Herein, an unsaturated version of BEDT–TTF, bis(vinylenedithio)tetrathiafulvalene (BVDT-TTF),[37–40] functionalized by four pyridines (**1**, Figure 1) was used as redox active ligand in combination with Cu(II), Zn(II), Cd(II) and Hg(II) to yield four isostructural coordination polymers frameworks as single crystals. After chemical oxidation of the frameworks *via* iodine doping, pronounced variation in conductivity was revealed in the case of **1**-$CdCl_2$ and **1**-$HgCl_2$. The oxidation states of the donor molecules in the series of new coordination polymers have been investigated by single-crystal Raman spectroscopy in both the neutral and oxidized state, and band structure calculations have been performed based on the structural data.

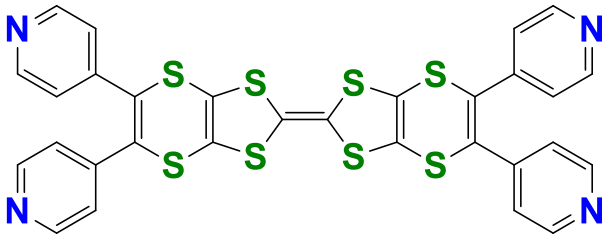

Figure 1. Tetra-pyridine bis(vinylenedithio)tetrathiafulvalene (BVDT-TTF-Py_4) **1**.

RESULTS AND DISCUSSIONS

Synthesis and description of the networks

BVDT-TTF-Py_4 **1** was prepared according to the literature procedure,[41] starting by a Diels-Alder reaction between 1,2-di(pyridin-4-yl)ethyne[42] and 1,3-dithiolane-2,4,5-trithione.[43] After trans-chalcogenation with mercury acetate and subsequent phosphite mediated coupling, BVDT-TTF-Py_4 was obtained with an overall yield of 60%. Replacement of the ethylene bridge of BEDT-TTF by a vinylene one creates a more rigid structure and avoid the formation of diastereomers, which would be formed upon substitution of the ethylene bridge in BEDT-TTF.[44]

The crystalline MOFs were synthesized by slow diffusion at RT during five days: a solution of ligand in DCM (1 mg/mL) was placed in a tube, a buffer solution of DCM/MeOH 1/1 and a solution (1 mg/mL) of

metal ($CdCl_2$, $HgCl_2$, $ZnCl_2$) in MeOH were successively layered. The same procedure was used for the synthesis of **1**-$CuCl_2$ with the ligand dissolved in $CHCl_3$.

Single crystals suitable for SCXRD were obtained with the four different metals. The four networks were all isostructural (monoclinic $P2_1/c$, with medium values for a = 13 Å ; b = 9.6 Å ; c = 16.2 Å ; β = 94°, see SI for details). The structure of **1**-$ZnCl_2$ network is presented Figure 2. These four materials all have the same formula **1**-MCl_2 (M = Cu, Zn, Cd or Hg). The asymmetric unit contains half a ligand and half a metal centre. Additional non-coordinated solvent molecules are also observed in the structures.

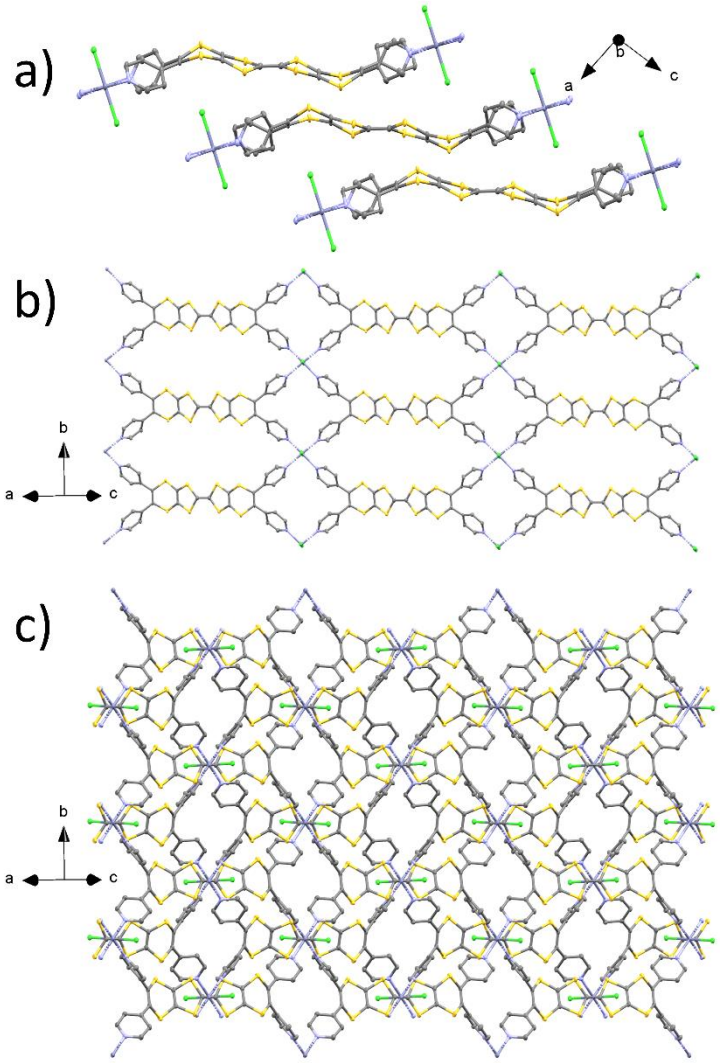

Figure 2.Single crystal X-ray structure for **1**-$ZnCl_2$. a) Side view of the BVDT-TTF stacking, b) view of a single 2D layer and c) packing (solvent molecules and H atoms have been omitted for the sake of clarity. C: grey ; S : yellow ; N : blue ; Cl : green and Zn : dark blue).

The metal atoms stand in an octahedral environment, with four pyridyl moieties forming the square base while two chlorine atoms are located in apical positions, with L-M-L angles in the 83 to 96° range (Table 1). The four pyridyl groups around one metal centre come from four different ligands. The metal-ligand distances are reported in Table 1. The longest M-Cl distance of 2.891 Å is observed for **1**-$CuCl_2$. The central C=C bonds are in the 1.34 Å range for **1**-$CuCl_2$, **1**-$ZnCl_2$ and **1**-$HgCl_2$, which is in the expected range for a non-oxidized TTF. The distance is slightly longer at 1.36(2)Å for **1**-$CdCl_2$, which is probably due to the uncertainty on the bond measurement. Additional Raman experiments (*vide infra*) did not show a characteristic peak for oxidized BVDT-TTF for pristine **1**-$CdCl_2$.

Table 1. Selected bond distances and angles for **1**-MCl_2. i and o correspond to the S atoms located on the inner rings and outer rings of **1**, respectively.

	Central C=C (Å)	M-N distance (Å)	M-Cl distance (Å)	N-M-N angle (°)	N-M-Cl angle (°)	Interligand S-S distance (Å)		
						i-i	i-o	i-o
1-$CuCl_2$	1.338(5)	2.062(3) – 2.085(3)	2.8907(9)	88.4 – 91.7	89.6 – 90.3	3.215(1)	3.759(1)	3.713(1)
1-$ZnCl_2$	1.350(5)	2.193(3) – 2.290(3)	2.4466(7)	85.2 – 94.8	90.0 – 90.4	3.249(1)	3.504(1)	3.707(1)
1-$CdCl_2$	1.36(2)	2.374(12) – 2.443(10)	2.563(3)	84.8 – 95.2	89.6 – 90.6	3.217(6)	3.556(5)	3.721(6)
1-$HgCl_2$	1.340(7)	2.437(3) – 2.547(3)	2.5286(10)	83.3 – 96.6	89.4 – 90.6	3.217(1)	3.516(1)	3.738(1)

The ligands are organized through coordination bonds in 2-D layers (Figure 2b) where metals are separated by 9.5-9.8 Å along the *b* axis, and 20.8-21.7 Å in the perpendicular direction. The layers are superimposed in a shifted fashion, the central C=C bond of the ligand in a 2-D layer standing below the metal centre of the following layer (Figure 2a and 2c). Between two ligands of different layers, the smallest S—S distance is in the 3.21 – 3.24 Å range in the four structures. 1-D channels are formed within the packing and are occupied by solvent molecules, representing *ca.* 30% of the overall crystal volume with pore size of 4.3 x 4.7 Å. The powdered crystals of **1**-$CuCl_2$, **1**-$CdCl_2$ and **1**-$HgCl_2$ preserve their crystallinity, as shown by PXRD after drying in the air at room temperature for 1 day (**see SI**), but the crystals of **1**-$ZnCl_2$ lost their crystalline character and only broad bands were observed by PXRD. Nevertheless, non-grinded single crystals are kept in the air several days without significant loss of diffraction intensity for all the materials.

In order to increase the overall conductivity of the materials, the presence of oxidized BVDT-TTF is necessary. Commonly, crystals are immerged in an iodine solution or exposed to iodine vapours. By exposure of **1**-MCl_2 dry crystals to I_2 vapours overnight, a stringent change of colour from red to dark purple is observed in every case, which is characteristic of the formation of oxidized thiafulvalenes. A loss of crystal quality is visually observed during the oxidation process. Interestingly, this change is reversible and the original colour is regenerated after one day. To our delight, crystals of **1**$^{\bullet+}$-$CdCl_2$-I_3^- have been formed in a single-crystal to single-crystal fashion and have been characterized by SCXRD despite a loss of data quality due to a decrease of the overall crystallinity. The network is in the *C*2/m space group, with cell parameters close to the parent **1**-$CdCl_2$ cell. A molecule of I_3^- has now replaced the solvent molecules within the pores, making the structure densely packed (Figure 3). Due to the lack of precision on the bond length, no characteristic lengthening of the central C=C bond is observed. PXRD were performed on the oxidized materials and present a proper match with the simulated spectra, although broad peaks indicate a possible loss of crystallinity (**see SI**).

Despite a change of the space group from $P2_1/c$ to *C*2/m, the overall structural arrangement of the ligands and metal is preserved between **1**-$CdCl_2$ and **1**$^{\bullet+}$-$CdCl_2$-I_3^- , both networks being practically superimposable. The unit cell parameters are similar +/- 2% in length and angles. The S-S interligand bond distances remain in the 3.2-3.7 Å range. The dihedral angles between the pyridyl and vinyl moieties changes from 51-57° to 88° between **1**-$CdCl_2$ and **1**$^{\bullet+}$-$CdCl_2$-I_3^-.

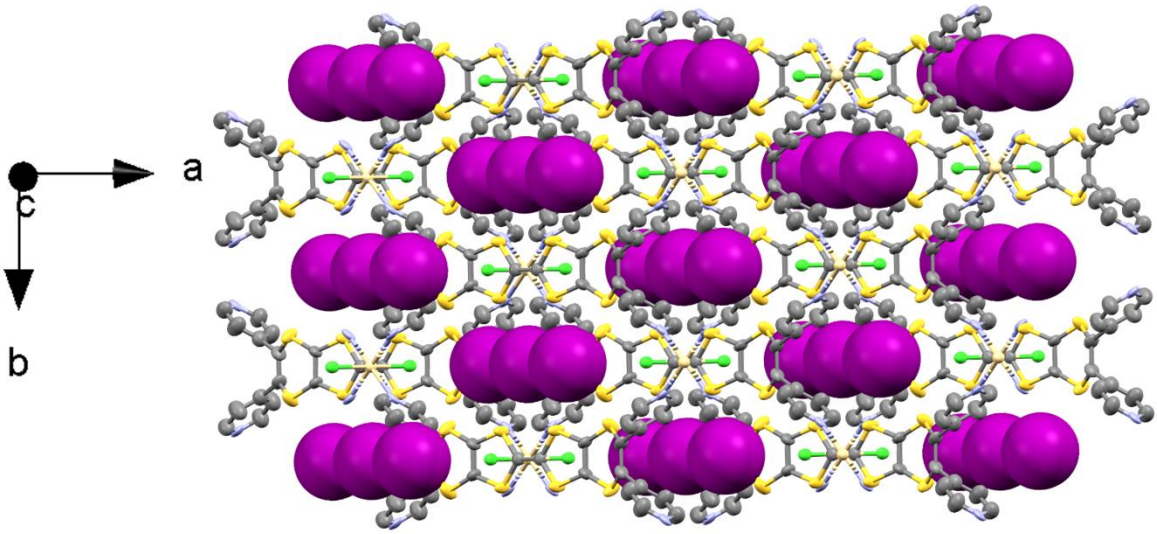

Figure 3. Single crystal X-ray structure for $\mathbf{1}^{\cdot+}$-$CdCl_2$-I_3^- along the c axis (H atoms have been omitted for the sake of clarity. C: grey ; S : yellow ; N : blue ; Cl : green ; Cd : light yellow and I : purple).

Solid-state cyclic voltammetry

Electrochemical-based cyclic voltammetry (CV) measurements were performed to analyze the redox process of MOF. A custom-designed setup was adopted since the MOFs are not soluble in any solvents. The approach is based on a solid-state electrochemical configuration described in the experimental part.

In the Table 2 are summarized the oxidation potential and reduction potential of Tetrapyridine BVDT–TTF **1**, **1**-$HgCl_2$, **1**-$CdCl_2$, **1**-$ZnCl_2$, **1**-$CuCl_2$. Cyclic voltammetry of the ligand (Figure 4) shows a pair of reversible redox waves centred at $E_{1/2}$ = 0.620(V) in a CH_2Cl_2 solution. The anodic peak of the ligand in solid state is at a lower voltage compared to those recorded in solution because of a slower diffusion process. It is indeed necessary to consider that the transport of electrons is probably limited to a tight region of the solid particles in contact with the electrode.[45] The broadness of the peak shape is also indicative of the high resistivity of the solid material. The values of the ligand are higher when compared with those of the related BEDT–TTF donor (whose first oxidation potential is $E_{1/2}$ = 0.49 V).

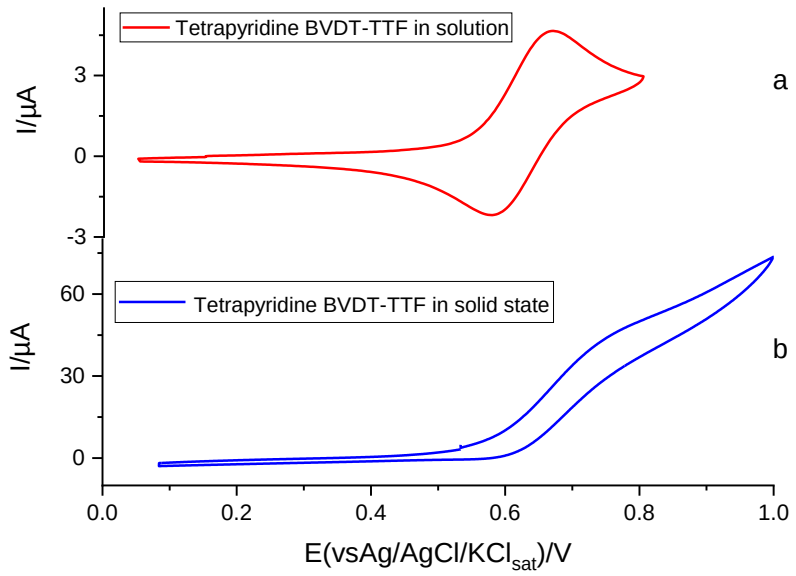

Figure 4. CV curves of a) 1 mM ligand in solution in 0.1 M $TBAPF_6$ DCM solution and (b) ligand powder with Nafion. WE/GCE for a) and GCP for b). RE: Ag/AgCl/KCl_{sat},. CE: Pt wire. CV profiles were obtained at 50 mV s^{-1} scan rate.

Table 2. Oxidation potential, E_{pa}, and reduction potential, E_{pc}, of **1**, **1**-$HgCl_2$, **1**-$CdCl_2$, **1**-$ZnCl_2$, **1**-$CuCl_2$ WE/GCE for a) and GCP for b). RE: Ag/AgCl/KCl_{sat}, CE: Pt wire.

	E_{pa} (V)	E_{pc} (V)
1 in solution	0.665	0.575
1 in solid state	0.75	0.61
1-$CuCl_2$ in solid state	0.66	0.40
1-$HgCl_2$ in solid state	0.74	0.62
1-$CdCl_2$ in solid state	0.73	0.62
1-$ZnCl_2$ in solid state	0.77	0.63

The CV curve of **1**-$HgCl_2$ (Figure 5, see SI for **1**-$CdCl_2$, **1**-$ZnCl_2$, **1**-$CuCl_2$) is selected to describe one quasi-reversible redox process corresponding to the formation of the BVDT-TTF radical cation at 0.74 V. In the case of MOFs, it is expected that the oxidation process will be extended along the entire solid particle thanks to the presence of pores allowing the passage of electrolyte species. Pore size therefore assumes a key role for redox conductivity. The redox properties of the ligand are therefore maintained in the structure of the four networks.

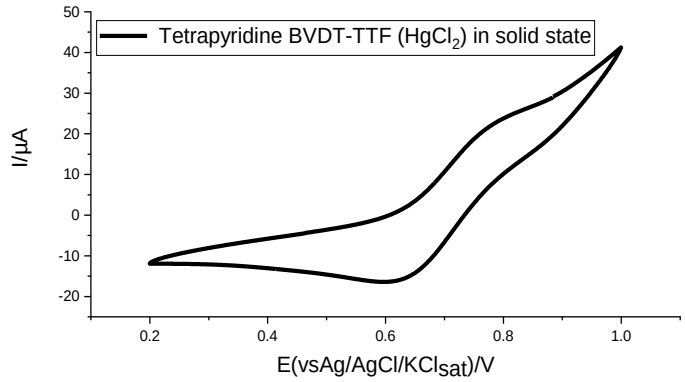

Figure 5. CV curve of **1**-$HgCl_2$ crystal powder coated with Nafion. WE: Glassy carbon plate. RE: Ag/AgCl/KCl_{sat},. CE: Pt wire ; 50 mV s^{-1} scan rate.

Raman spectroscopy

Raman spectroscopy experiments and theoretical calculations were performed to assess the oxidation state of BVDT-TTF in our compounds in the non-oxidized and oxidized species. The ligand **1** is characterized by strong σ-donating and π-accepting character[41] and the coordination bond between pyridine and metal is responsible for notable cooperative electronic properties of the resulting material.

C=C stretching modes of **1** usually observed in Raman spectra stands in the frequency range 1300 – 1700 cm^{-1}. These modes are known to display a strong dependence of frequency on charge and have been widely used in characterization of charge states in BEDT-TTF-based salts.[46,47]

DFT calculations of vibrational modes for both the neutral **1** and the radical cation $\mathbf{1}^{\bullet+}$ have been performed in order to estimate the charge localized on **1** in the selected-based coordination polymers. Charge-sensitive vibrations can be used to determine the charge state. The tetrapyridine-substituted BVDT-TTF molecule, based on the fully unsaturated version of BEDT–TTF,[41] is not flat but assume an approximately orthogonal orientation with respect to the main molecular plane. This is clearly seen in Figure 6 that displays comparison of the frontier molecular orbitals in the neutral and the cation.

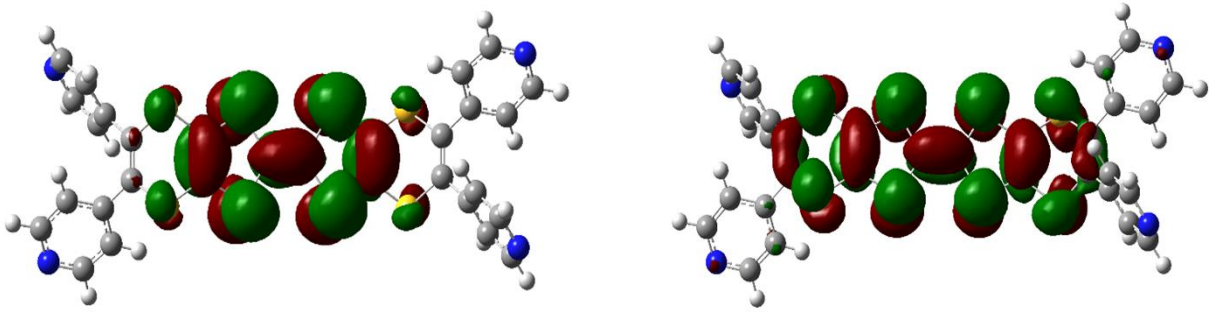

Figure 6. Frontier molecular orbitals: HOMO (Highest Occupied Molecular Orbital) of neutral BVDT-TTF-Py_4 (left), and α-SOMO (Single Occupied MO) of the BVDT-TTF-$Py_4^{\bullet+}$ cation (right), calculated using DFT methods.

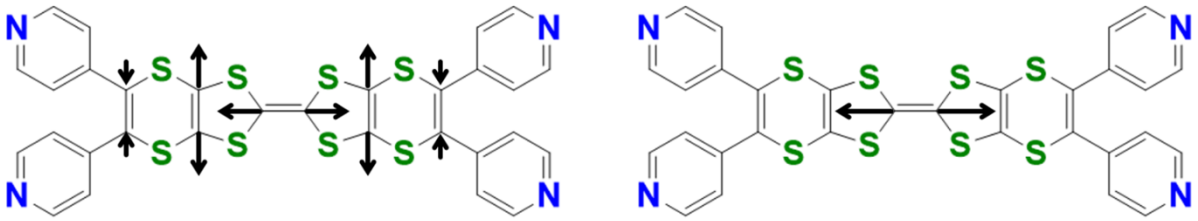

Figure 7. Schematic view of the symmetric C=C stretching ν_C mode of the neutral BVDT-TTF-Py$_4$ molecule (left) and BVDT-TTF-Py$_4^{\bullet+}$ radical cation (right), as it results from DFT calculations.

As a consequence of this steric arrangement, molecular dynamics of **1** significantly differs between the neutral and the cation. The charge-sensitive vibration mode labelled ν_C (Figure 7) displays the strongest frequency dependence on charge. In case of the neutral **1**, the ν_C mode features in-phase stretching of the three inner double C=C bonds, but the vibration is confined to the central C=C bond for the cation. The theoretical frequency of ν_C is 1500 cm^{-1} for the neutral and 1382 cm^{-1} for the cation, therefore we observe similar frequency shift of the charge-sensitive mode due to oxidation of the donor molecule as the value characteristic for charge-sensitive modes of BEDT-TTF.[46]

Figure 8 shows Raman spectra measured at room temperature for selected coordination polymers based on neutral **1**, together with the experimental and theoretical Raman spectrum of the neutral **1**. The characteristic vibrational structure in the frequency range of the stretching C=C modes is clearly seen in all experimental spectra, in close agreement with the theoretical spectrum. We assign the strong band centred at 1500 cm^{-1} in the theoretical spectrum of neutral **1**, and in the range 1503-1514 cm^{-1} in experimental spectra, as the charge-sensitive ν_C mode characteristic for the neutral species (Table 3). The presence of a broad feature at 1410 cm^{-1} in **1**-$HgCl_2$ and at 1414 cm^{-1} in **1**-$ZnCl_2$, that we attribute to ν_C of the cation, suggests that a minute amount of BVDT-TTF(Py)$_4^{\bullet+}$ radicals is present in these materials. Note that in theoretical spectra, Raman intensity at the frequency of ν_C is two order of magnitude higher in case of the cation than in case of the neutral donor.

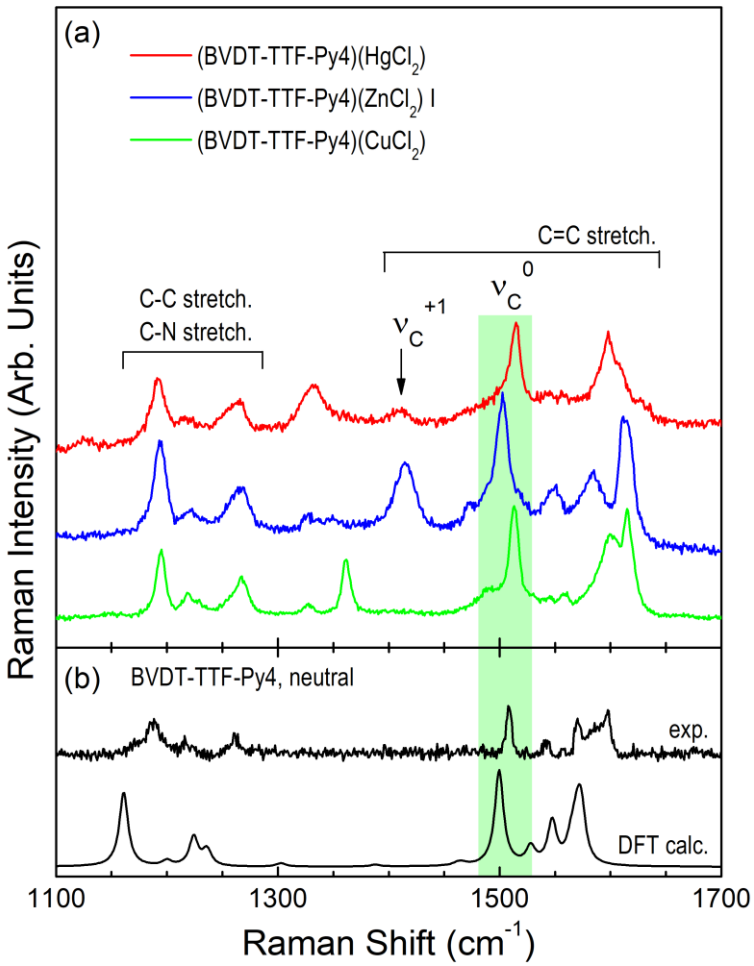

Figure 8. (a) Raman spectra of selected BVDT-TTF(Py)$_4$ coordination polymers measured at room temperature with the 785 nm excitation line; (b) room temperature Raman spectrum of neutral **1** measured with the 785 nm excitation line, together with the respective theoretical Raman calculated at the B3LYP/6-31++G(d,p) level of theory. Note that the spectra in both panels are offset for clarity; the charge-sensitive ν_C mode is labelled as ν_C^0 for the neutral and ν_C^{+1} for the cation.

In the theoretical spectrum of BVDT-TTF-Py$_4^+$ (Figure 9b) the charge-sensitive ν_C mode, identified as a signature of the cation, appears as a strong band centred at 1382 cm^{-1}. In the experimental Raman spectra, this mode is located at 1402 in **1**$^{\cdot+}$-$CdCl_2$-I_3^- (Table 3). On the other hand, the relatively weak feature centred at 1503 cm^{-1} is suggestive of remaining neutral BVDT-TTF(Py)$_4$ molecules in the structure (Table 3).

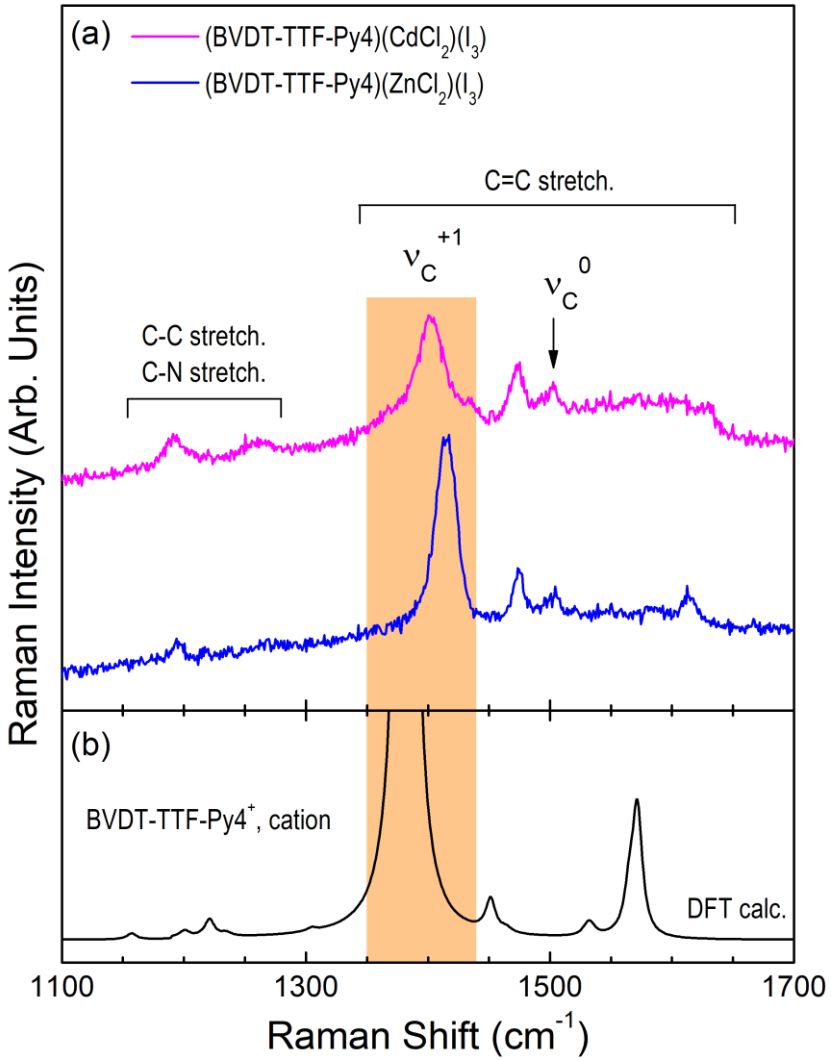

Figure 9. (a) Raman spectra of **1**$^{\bullet+}$-$CdCl_2$-I_3^- measured at room temperature with the 785 nm excitation line. (b) Theoretical Raman spectrum of **1**$^{\bullet+}$ calculated at the B3LYP/6-31++G(d,p) level of theory. The spectra in panel (a) are offset for clarity; the charge-sensitive ν_C mode is labelled as ν_C^{+1} for the cation.

Table 3. The positions in cm^{-1} of the charge-sensitive ν_C mode in calculated and experimental Raman spectra of **1** and coordination polymers with M = Zn, Hg, Cu, and (**1**$^{\bullet+}$-$CdCl_2$-I_3^-), with M = Cd, Zn.

	DFT calc[a]/ Neutral exp.	**1**-$ZnCl_2$	**1**-$HgCl_2$	**1**-$CuCl_2$	**1**-$CdCl_2$-I_3^-
ν_C^0	1500/1509	1503	1515	1513	1503
ν_C^{+1}	1382/-	1414	1410	-	1402

[a] theory level: B3LYP/6-31++G(d,p), scaled with 0.9614 factor

Single-crystal resistivity measurements

Conductivity measurements were performed with a two-contact method on single crystals for compounds **1**-$CdCl_2$ and **1**-$HgCl_2$ before and after oxidation. **1**-$CuCl_2$ and **1**-$ZnCl_2$ crystals were too small for connection with the electrodes. For **1**-$HgCl_2$ the conductivity goes from 2 - $2.5\cdot10^{-9}$ $S\cdot cm^{-1}$ to 1.2 - $2\cdot10^{-8}$ $S\cdot cm^{-1}$ upon oxidation and for **1**-$CdCl_2$ from 7 - $9\cdot10^{-10}$ $S\cdot cm^{-1}$ to 4 - $6\cdot10^{-9}$ $S\cdot cm^{-1}$ (2 crystals measured for each compound). This *ca.* 8-fold enhancement of the conductivity for both compounds is directly related to the partial oxidation of the ligands, yielding an open-shell structure, and may be partly counter-balanced by the loss of crystallinity observed in X-ray.

Band structure calculations

The electronic delocalization in the present coordination networks occurs essentially via direct through-space S···S contacts within the (BVDT-TTF-Py_4) sublattice. As shown in Figure 10a where the short S···S contacts are shown as dotted red lines, the conductive path is confined within ab layers well separated by $CdCl_2$ and the pyridine ligands (and solvent molecules, not shown). These layers (Figure 10b) result from the superposition of two layers as those in Figure 2b. These layers are in fact step-layers (Figure 10d) where every step is made of a series of equivalent donors along b. As schematically shown in Figure 10d, the molecules of successive steps turn around opposite directions. Note that step-layers are in fact the conductive components of many molecular conductors and superconductors.[48] Although the a- and c-directions are interchanged, the same description applies for $\mathbf{1}^{\bullet+}$-$CdCl_2$-I_3^-. These step-layers ensure a 2D continuous path of S···S interactions through the overlap mode in Figure 10c and should make the present networks relatively immune to defects.

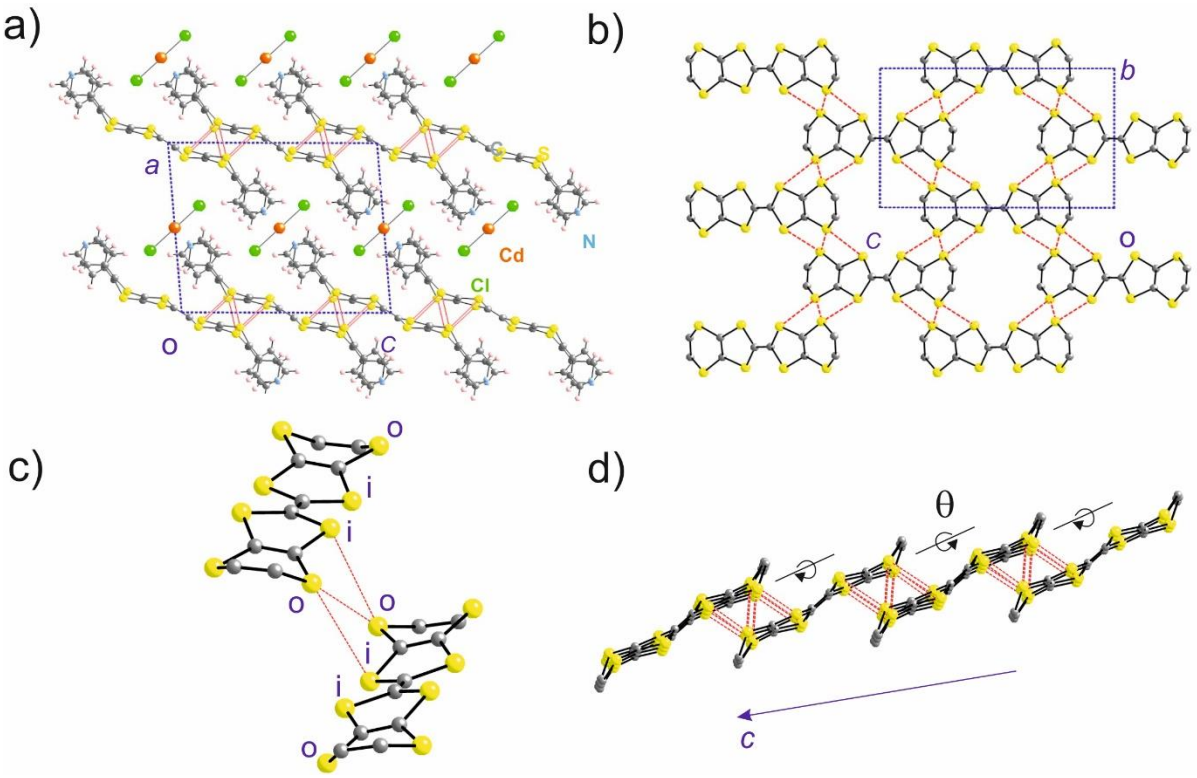

Figure 10. Crystal structure of **1**-$CdCl_2$ where the short S···S contacts are shown as red dotted lines; for clarity solvent molecules are not displayed and the pyridine ligands have been omitted in b), c) and d). a) Projection view along the b-direction, b) Overlap mode between pairs of **1** donors where the inner (i) and outer (o) types of S atoms are noted, c) top view of a double layer, and d) schematic lateral view showing that the double layers are step-layers with successive steps built from donors turning in opposite senses.

The calculated DFT band structure for **1**-$CdCl_2$ is shown in Figure 11a where the energy zero refers to the highest occupied level of the HOMO band. It is the typical band structure of a slightly direct band gap semiconductor with hole type conductivity. The HOMO band is folded along the b*- and c*-directions because there are two equivalent molecules in the repeat unit. It exhibits similar dispersion along both the c* (Γ-Z) and b* (Γ-Y) directions, *i.e*. is a typical 2D band. The total dispersion is ~ 0.3 eV which is not far from that of some of the most studied conducting metal-organic frameworks like Zn_2(TTFTB) [H_4TTFTB= tetrathiafulvalene tetrabenzoic acid], ~ 0.4 eV.[20] The band gap of the two systems are also quite comparable, 1.47 eV for **1**-$CdCl_2$ and 1.75 eV for Zn_2(TTFTB). It is interesting to compare the results for the two frameworks even if the first is electronically 2D whereas the second is 1D. The shortest S···S contact in the present compound is 3.217 Å which is considerably shorter than in Zn_2(TTFTB), 3.757 Å. It is therefore surprising that the band dispersion is somewhat smaller for **1**-$CdCl_2$. Despite intrinsic orbital orientation aspects fixed by the coordination network there is another important aspect worth of notice. In the extended BVDT-TTF donor there are two types of S atoms: those of the inner TTF core and those which are out of this core (noted "i" and "o" respectively in Figure 10c). It is well known for similar ligands like ET [bisethylenedithiatetrathiafulvalene] (see also Figure 6 left) that the participation of the outer S p_z orbitals into the HOMO is noticeably smaller than that of the inner S ones (for ET the relation is around 1/3).[48,49] In the case of Zn_2(TTFTB) the contacts are of the i···i type but in the present case the 3.217 Å contact is of the o···o type (see Figure 10c) and the two other contacts, 3.546 and 3.721 Å are of the i···o type. Thus, the S···S contacts are less effective than in Zn_2(TTFTB) because they all implicate S atoms of the o type but there are more numerous and finally the band dispersion is only a bit smaller. These contacts can be tuned for instance varying the angle θ (see Figure 10d) or the nature of the transition metal. We believe that using these more extended donors, step-layers with band dispersion comparable to those in the M_2(TTFTB) family and other frameworks where the conducting path is mostly 1D can be reached and tuned. In addition, because of the 2D conducting path, the conductivity will be more stable and immune to defects.

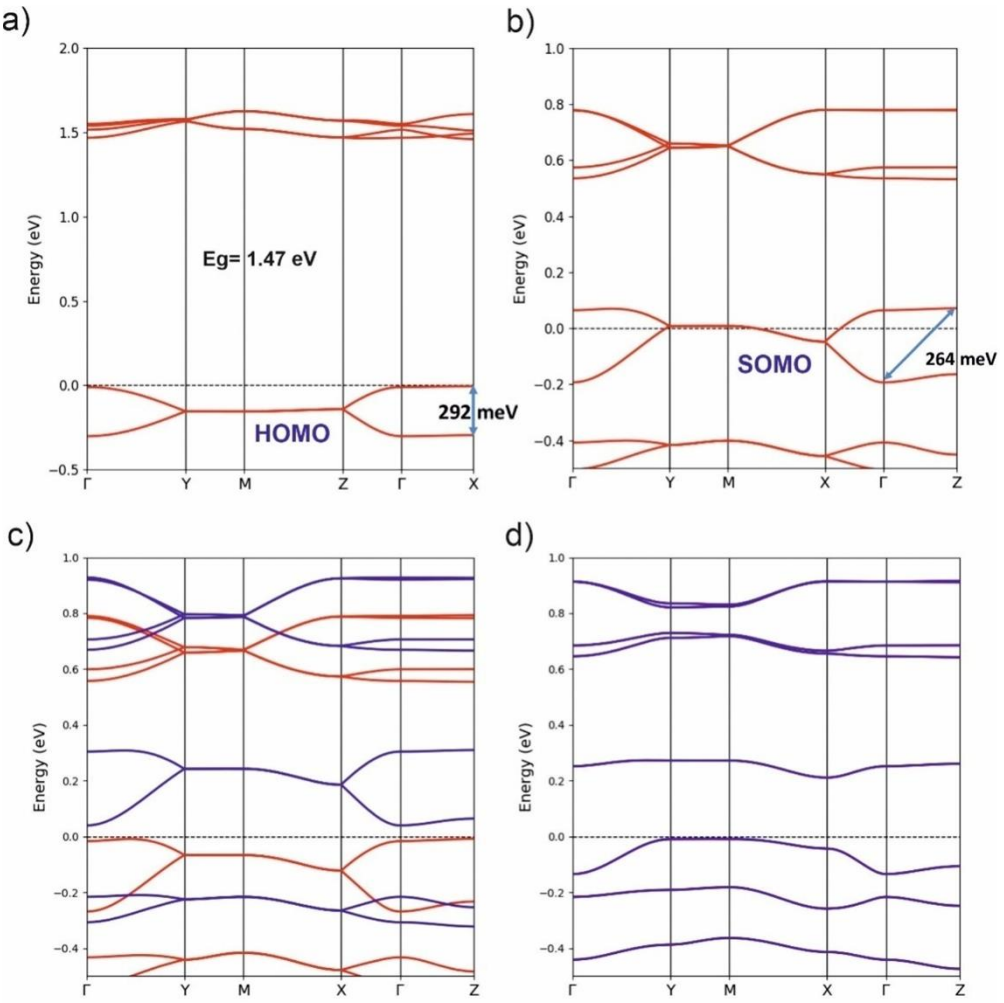

Figure 11.DFT band structure for **1**-$CdCl_2$ (a). DFT band structure for the metallic (b), ferromagnetic (c) and fully antiferromagnetic states (d) of **1**$^{\bullet+}$-$CdCl_2$-I_3^-. Γ = (0, 0, 0), X = (a*/2, 0, 0), Y = (0, b*/2, 0) and Z = (0, 0, c*/2); M = (0, b*/2, c*/2) in a) but (a*/2, b*/2, 0) in b), c) and d). The dashed line refers to the highest occupied level in all cases. All levels up to the energy zero are doubly filled in a) and b). Spin-up and spin-down bands are shown in red and blue, respectively in (c) and (d). The spin-up and spin-down bands are identical although located in spatially different but equivalent sites in (d) so that they superpose and only the blue bands are visible. Note the larger energy scale in a).

The calculated DFT band structure for **1**$^{\bullet+}$-$CdCl_2$-I_3^- assuming double occupation of the levels (i.e., a metallic state) is shown in Figure 11b. Now the HOMO band is half-filled and the Fermi level lies inside the band. The important feature is that the topology of this SOMO band is similar to that of the HOMO band for the non-oxidized donor lattice and the total dispersion is also comparable (264 meV in Figure 11b and 292 meV in Figure 11a. Note the larger energy scale in Figure 11a). Consequently, the nature of the S···S interactions already discussed has not experienced a major disturbance upon the oxidation of the donor lattice. The major change concerns the energy separation between the SOMO and the lower fully empty bands but this does not play any important physical role for **1**$^{\bullet+}$-$CdCl_2$-I_3^-. Since the band is half-filled and given the stoichiometry, the electronic structure for situations

where every donor accommodates a single localized electron must be considered. In Figures 11c and 11d are shown the DFT band structures for localized states where all donors have an electron with the same spin i.e. a ferromagnetic state (FM), or where all adjacent donors have opposite spins, i.e. a fully antiferromagnetic state (AF). The metallic state was found to be higher in energy (in meV/formula unit) than both the FM and full AF states: Metallic (0), FM (-23.8) and full AF (-34.0), thus confirming the electronically localized nature of $\mathbf{1}^{\bullet+}$-$CdCl_2$-I_3^-. This system should therefore exhibit an antiferromagnetic ground state.

The effect of electronic repulsions is clearly seen comparing the band structures of the metallic (Figure 11b) and FM (Figure 11c) states. The spin up (red) and spin down (blue) bands of the FM state are shifted almost rigidly and have the same shape as those in the metallic state. Because of the electron repulsions, a gap develops separating the filled and empty bands so that the conductivity is activated. However, the gap is of a considerably different nature that that occurring in **1**-$CdCl_2$ (Figure 11a) and is dominated by the electron-electron repulsions within the SOMO of the donors, which outweigh the effect of the direct S···S overlap. The bands for the more stable full AF state (Figure 11d) are really the superposition of two bands (one mostly associated with spin up and more localized in the donors of one out of every two steps of the layer while the other, with spin down, is more localized in the donors of the other step). The more favorable electron-electron repulsions in the fully AF state lead to the opening of a very noticeable gap between flatter bands as a result of the spatial confinement of electrons with different spins into different steps of the layer. We have checked that other spin configurations within the step-layer do not lead to energies lower than that of the full AF state by carrying out calculations using a doubled unit cell along the a- and b- directions. Calculations using double cells along the interlayer c-direction led to energy differences of the order of less than 1 K per formula unit, which are within the energy error of the calculations, and thus, we believe that there is no magnetic order between layers. Because of the intercrossed nature of the 2D interactions, it is not likely that the conducting and magnetic properties are seriously disturbed by the presence of a small number of non-oxidized donors.

In summary, the use of extended TTF-based donors such as **1** may lead to interesting new conducting coordination networks mostly because of two features: (i) they favor 2D conducting paths which will make these systems considerably less sensitive to defaults, and (ii) the extended nature of the sulfur-containing fragment of the donor decreases the U intra-site electron repulsion term (*i.e.* the U_{SOMO}) which dominates the activation energy. Further engineering of the conductivity can also be anticipated by controlling the S···S contacts, as noted above, that will play on the overlap component of the hopping.

CONCLUSIONS

In conclusion, four unprecedented isostructural networks have been synthesized by the self-assembly of a BVDT-TTF substituted with four pyridyl moieties and a MCl_2 metal centre (M = Cu, Zn, Cd, Hg). The networks present solvent occupied pores and are oxidized post-synthetically by exposition to I_2 vapours. For the oxidation of **1**-$CdCl_2$ to $\mathbf{1}^{\bullet+}$-$CdCl_2$-I_3^- , the reaction occurred in a single crystal to single crystal fashion and was followed by SCXRD. Room temperature Raman study of a series of new coordination polymers based on **1** supports the observed charge of the ligand within the networks. In the frequency range of the stretching C=C modes, a charge-sensitive ν_C mode is identified with the

help of theoretical calculations using DFT methods. Raman confirmed the oxidized state of the ligand in the bulk crystals. An 8-fold enhancement of conductivity was measured on single crystals of **1**-$CdCl_2$ and **1**-$HgCl_2$ after oxidation. Band structure calculations unveiled the 2D nature of the conducting path so that these systems should be unsensitive to defaults. The calculations suggest an antiferromagnetic ground state for the conducting layers but no magnetic order between layers. Cyclic voltammetry performed on bulk powder show that the redox properties of the ligand are maintained for all MOFs. This study demonstrates the relevance of the utilization of TTF based ligands possessing additional sulphur atoms in the design of conductive networks thanks to the formation of 2D conductive pathways. In this regard, it is important to implement the wide variety of electroactive structures found for organic conductors within MOFs scaffolds, which is the main direction of our current researches.

EXPERIMENTAL SECTION

Ligand **1** was synthesized according to reported literature procedures.[41]

1-$ZnCl_2$ synthesis:

Ligand **1** (1 mg, $1.54x10^{-3}$ mmol) was dissolved in 1 ml of DCM and placed in a tube (13 cm height, 1 cm diameter). A buffer solution of DCM/MeOH 1/1 (0.5 mL) and a solution of metal $ZnCl_2$ (2 mg, 0.014 mmol) in MeOH (2 mL) were successively layered. After 5 days, red crystals appeared. The crystals were washed several times with ethanol and DCM. $C_{30}H_{16}N_4S_8\,Cl_2Zn$, 3($CH_2Cl_2$) theor. : C, 36.70; H, 2.05; N, 5.19; S, 23.75. Found: C, 35.05 H, 1.74; N, 5.12; S, 25.13.

1-$CuCl_2$ synthesis:

Ligand **1** (1 mg, $1.54x10^{-3}$ mmol) was dissolved in 1 ml of $CHCl_3$ and placed in a tube (13 cm height, 1 cm diameter). A buffer solution of $CHCl_3$/MeOH 1/1 (0.5 mL) and a solution of metal $CuCl_2$ (2 mg, 0.014 mmol) in MeOH (2 mL) were successively layered. After 5 days, red crystals appeared. The crystals were washed several times with ethanol and $CHCl_3$. $C_{30}H_{16}N_4S_8Cl_2Cu$, ($CHCl_3$) theor.: C, 39.49; H, 1.82; N, 5.94; S, 27.21. Found: C, 39.58; H, 1.96; N, 5.63; S, 27.43.

1-$CdCl_2$ synthesis:

Ligand **1** (1 mg, $1.54x10^{-3}$ mmol) was dissolved in 1 ml of DCM and placed in a tube (13 cm height, 1 cm diameter). A buffer solution of DCM/MeOH 1/1 (0.5 mL) and a solution of metal $CdCl_2$ (2 mg, 0.010 mmol) in MeOH (2 mL) were successively layered. After 5 days, red crystals appeared. The crystals were washed several times with ethanol and DCM. $C_{30}H_{16}N_4S_8Cl_2Cd$, 2(CH_2Cl_2) theor.: C, 36.88; H, 1.93; N, 5.38; S, 24.61. Found: C, 36.40; H, 1.88; N, 5.20; S, 25.67.

1-$HgCl_2$ synthesis:

Ligand **1** (1 mg, $1.54x10^{-3}$ mmol) was dissolved in 1 ml of DCM and placed in a tube (13 cm height, 1 cm diameter). A buffer solution of DCM/MeOH 1/1 (0.5 mL) and a solution of metal $HgCl_2$ (2 mg, $7.36x10^{-3}$ mmol) in MeOH (2 mL) were successively layered. After 5 days, red crystals appeared. The crystals were washed several times with ethanol and DCM. $C_{30}H_{16}N_4S_8Cl_2Hg$, (CH_2Cl_2) theor. : C, 35.62; H, 1.74; N, 5.36; S, 24.54. Found: C, 34.53; H, 1.67; N, 5.05; S, 24.70.

General procedure for the post-synthetic oxidation. 10 mg of **1**-MCl_2 were deposited in a 2 mL vial. It was placed in a larger vial containing I_2 (*ca.* 50 mg), the vial was closed and left overnight at room temperature. A colour change from red to dark purple is observed in every case. The crystals were used as such for the subsequent measurements.

X-Ray structure determinations

Details about data collection and solution refinement are given in Table S1. Data collections were performed on a Rigaku Oxford Diffraction SuperNova diffractometer equipped with an Atlas CCD detector and micro-focus Cu-K_α radiation (λ = 1.54184 Å). The structures were solved by intrinsic phasing and refined on F^2 by full matrix least-squares techniques with SHELX programs (SHELXT 2018/2 and SHELXL 2018/3)[50,51] using the ShelXle and the Olex2 graphical user interfaces.[52,53] All non-H atoms were refined anisotropically and absorption was corrected by multiscan empirical absorption using spherical harmonics with CrysAlisPro program for **1**-$CuCl_2$, **1**-$ZnCl_2$, **1**-$CdCl_2$ and **1**-$HgCl_2$. The H atoms were placed at calculated positions and refined using a riding model. Crystallographic data for the five structures have been deposited with the Cambridge Crystallographic Data Centre, deposition numbers CCDC for **1**-$CuCl_2$: 2203496; **1**-$ZnCl_2$: 2203494 ; **1**-$CdCl_2$: 2203493; **1**-$HgCl_2$: 2203497; **1**-$CdCl_2$-I_3 : 2203495.These data can be obtained free of charge from CCDC, 12 Union road, Cambridge CB2 1EZ, UK (e-mail: deposit@ccdc.cam.ac.uk or http://www.ccdc.cam.ac.uk).

Solid state cyclic voltammetry

To measure solid state electrochemical behaviour of MOFs, a cylindrical Teflon cell featuring a hole (0.4 cm diameter) in the bottom was used in a vertical configuration, where a glassy carbon plate as working electrode, WE, was tightened from below. The cell was tightened on a copper plate as the electrical contact. A Pt wire and Ag wire were used as counter electrode (CE) and reference electrode (RE) respectively and placed at the top of the cylinder in contact with the electrolytic solution (0.1M $TBAPF_6$in AN) vs *Fc+/Fc*. The MOFs were placed over the WE and covered with a Nafion membrane, to prevent direct contact between the solid MOFs and the electrolytic solution.

Computational methods

Theoretical calculations of normal vibrational modes for BVDT-TTF-Py_4 isolated molecule were performed with Gaussian 03,[54] using the standard 6-31++G(d,p) basis set and the hybrid density functional (B3LYP). The initial geometry used in calculations was prepared based on the experimental X-ray data. The result of the structure optimization corresponds to energy minima since no imaginary frequencies were found. On the basis of optimized structure, vibrational frequencies as well as Raman scattering activities were calculated. The frequencies computed with a quantum harmonic oscillator approximation tend to be higher than experimental ones, and the scaling factor 0.9614 has been applied.[55]

Band structure calculations

The first-principles calculations for the solid were carried out using a numeric atomic orbitals density functional theory (DFT) approach[56,57] developed for efficient calculations in large systems and implemented in the SIESTA code.[58–61] We used the generalized gradient approximation (GGA) to DFT and, in particular, the functional of Perdew, Burke, and Ernzerhof.[62] To study the relative energies of states with localized electrons, spin polarized band calculations have been undertaken. All calculations included a Hubbard correction term $U_{eff} = U - J = 6.0$ eV for the S 3p states.[63] In previous work[64] we have found that this U term on the chalcogen atoms is needed for appropriately describing the electronic structure of molecular conductors were accurate experimental information on the bandwidth and charge transfer is available. Only the valence electrons are considered in the calculation, with the core being replaced by norm-conserving scalar relativistic pseudopotentials[65] factorized in the Kleinman–Bylander form.[66] We have used a split-valence double-ζ basis set including polarization orbitals with an energy shift of 10 meV for S, C, N, Cl, Cd and H atoms.[67] The energy cut-off of the real space integration mesh was 350 Ry. The Brillouin zone was sampled using grids of (7×7×7) k-points.[68] The experimental crystal structures for (BVDT-TTF-Py_4)-$CdCl_2$ and (BVDT-TTF-Py_4)$^{\cdot+}$-$CdCl_2$-I_3^- were used for the computations.

Raman measurements

Crystalline samples selected for Raman measurements were between 0.1 and 0.2 mm in length. Raman spectra in the range 1100 – 1700 cm^{-1} were measured at room temperature using Renishaw inVia Raman microscope equipped with a thermoelectrically (TE)-cooled CCD detector and semiconductor laser emitting light in near-infrared region at 785 nm wavelength. Low-frequency Raman spectra were measured at room temperature in a backward scattering geometry with a LABRAM HR800 Raman spectrometer equipped with a microscope and a He-Ne λ=632.8 nm laser line. The spectral resolution of Raman measurements was better than 2 cm^{-1}, and the power was reduced to about 0.3 mW to avoid sample overheating.

Conductivity measurements

Electrical conductivity measurements at room temperature were performed in two points on 0.2 to 0.3mm long single crystals. Gold wires were glued with silver paste on both ends of the crystals. We have used a Keithley 486 picoammeter to apply a constant voltage (up to 30V) and measure the current, leading to resistance values of the order of 100GΩ.

Acknowledgements

This work was supported in France by the CNRS and the University of Angers (PhD funding to F.S.). N.A. and I.O. thank the Narodowa Agencja Wymiany Akademickiej – NAWA (Poland, BPN/BFR/2021/1/00001/U/00001) and the French Ministry of Foreign Affairs and the French Ministry of Education and Research (France, PHC Project 48119PG) for financial support through the bilateral Polonium project. The work in Poland was supported within the Statutory Activities of the Institute of Molecular Physics Polish Academy of Sciences and partially supported at Poznan University of Technology by the Research Project of the Polish Ministry of Education and Science 0511/SBAD/2251. Work in Spain was supported by MICIU through Grants PGC2018-096955-B-C44 and PGC2018-093863-B-C22, and Generalitat de Catalunya (2017SGR1506 and 2017SGR1289). E.C. acknowledges support of the Spanish MICIU through the Severo Ochoa FUNFUTURE (CEX2019-000917-S) Excellence Centre distinction and P. A. from the Maria de Maeztu Units of Excellence Program (MDM-2017-0767).

Keywords

Conducting Materials

Crystal engineering

Metal-organic frameworks

Raman spectroscopy

X-ray diffraction

References

[1] N. P. Brandon, D. J. Brett, *Philos. Trans. A Math. Phys. Eng. Sci.* **2006**, *364*, 147–159.
[2] Y. Ren, G. H. Chia, Z. Gao, *Nano Today* **2013**, *8*, 577–597.
[3] S. Kondrat, C. R. Pérez, V. Presser, Y. Gogotsi, A. A. Kornyshev, *Energy Environ. Sci.* **2012**, *5*, 6474–6479.

[4] H.-C. “Joe” Zhou, S. Kitagawa, *Chem. Soc. Rev.* **2014**, *43*, 5415–5418.
[5] N. Stock, S. Biswas, *Chem. Rev.* **2012**, *112*, 933–969.
[6] J.-R. Li, R. J. Kuppler, H.-C. Zhou, *Chem. Soc. Rev.* **2009**, *38*, 1477-1504.
[7] M. C. Das, S. Xiang, Z. Zhang, B. Chen, *Angew. Chem. Int. Ed.* **2011**, *50*, 10510–10520.
[8] J. D. Evans, C. J. Sumby, C. J. Doonan, *Chem. Soc. Rev.* **2014**, *43*, 5933–5951.
[9] Y.-B. Huang, J. Liang, X.-S. Wang, R. Cao, *Chem. Soc. Rev.* **2017**, *46*, 126–157.
[10] N. Hanikel, M. S. Prévot, F. Fathieh, E. A. Kapustin, H. Lyu, H. Wang, N. J. Diercks, T. G. Glover, O. M. Yaghi, *ACS Cent. Sci.* **2019**, *5*, 1699–1706.
[11] L. Liu, Y. Zhou, S. Liu, M. Xu, *ChemElectroChem* **2018**, *5*, 6–19.
[12] K. J. Erickson, F. Léonard, V. Stavila, M. E. Foster, C. D. Spataru, R. E. Jones, B. M. Foley, P. E. Hopkins, M. D. Allendorf, A. A. Talin, *Adv. Mater.* **2015**, *27*, 3453–3459.
[13] G. Xu, P. Nie, H. Dou, B. Ding, L. Li, X. Zhang, *Mater. Today* **2017**, *20*, 191–209.
[14] L. S. Xie, G. Skorupskii, M. Dincă, *Chem. Rev.* **2020**, *120*, 8536–8580.
[15] E. M. Johnson, S. Ilic, A. J. Morris, *ACS Cent. Sci.* **2021**, *7*, 445–453.
[16] L. Qu, H. Iguchi, S. Takaishi, F. Habib, C. F. Leong, D. M. D’Alessandro, T. Yoshida, H. Abe, E. Nishibori, M. Yamashita, *J. Am. Chem. Soc.* **2019**, *141*, 6802–6806.
[17] A. T. Castner, H. Su, E. Svensson Grape, A. K. Inge, B. A. Johnson, M. S. G. Ahlquist, S. Ott, *J. Am. Chem. Soc.* **2022**, *13*, 5910–5920.
[18] J. Huang, Y. He, M.-S. Yao, J. He, G. Xu, M. Zeller, Z. Xu, *J. Mater. Chem. A* **2017**, *5*, 16139–16143.
[19] G. Skorupskii, K. N. Le, D. L. M. Cordova, L. Yang, T. Chen, C. H. Hendon, M. Q. Arguilla, M. Dincă, *PNAS* **2022**, *119*, e2205127119.
[20] S. S. Park, E. R. Hontz, L. Sun, C. H. Hendon, A. Walsh, T. Van Voorhis, M. Dincă, *J. Am. Chem. Soc.* **2015**, *137*, 1774–1777.
[21] A. Fateeva, J. Clarisse, G. Pilet, J.-M. Grenèche, F. Nouar, B. K. Abeykoon, F. Guegan, C. Goutaudier, D. Luneau, J. E. Warren, M. J. Rosseinsky, T. Devic, *Cryst. Growth Des.* **2015**, *15*, 1819–1826.
[22] T. L. A. Nguyen, R. Demir-Cakan, T. Devic, M. Morcrette, T. Ahnfeldt, P. Auban-Senzier, N. Stock, A.-M. Goncalves, Y. Filinchuk, J.-M. Tarascon, G. Férey, *Inorg. Chem.* **2010**, *49*, 7135–7143.
[23] T. C. Narayan, T. Miyakai, S. Seki, M. Dincă, *J. Am. Chem. Soc.* **2012**, *134*, 12932–12935.
[24] Y. Zhou, Q. Hu, F. Yu, G.-Y. Ran, H.-Y. Wang, N. D. Shepherd, D. M. D’Alessandro, M. Kurmoo, J.-L. Zuo, *J. Am. Chem. Soc.* **2020**, *142*, 20313–20317.
[25] H. Banda, J.-H. Dou, T. Chen, N. J. Libretto, M. Chaudhary, G. M. Bernard, J. T. Miller, V. K. Michaelis, M. Dincă, *J. Am. Chem. Soc.* **2021**, *5*, 2285–2292.
[26] T. Devic, D. Rondeau, Y. Şahin, E. Levillain, R. Clérac, P. Batail, N. Avarvari, *Dalton Trans.* **2006**, 1331–1337.
[27] D. Lorcy, N. Bellec, M. Fourmigué, N. Avarvari, *Coord. Chem. Rev.* **2009**, *253*, 1398–1438.
[28] H.-Y. Wang, J.-Y. Ge, C. Hua, C.-Q. Jiao, Y. Wu, C. F. Leong, D. M. D’Alessandro, T. Liu, J.-L. Zuo, *Angew. Chem. Inter. Ed.* **2017**, *56*, 5465–5470.
[29] H.-Y. Wang, Y. Wu, C. F. Leong, D. M. D’Alessandro, J.-L. Zuo, *Inorg. Chem.* **2015**, *54*, 10766–10775.
[30] Q. Yu, J. Su, J.-P. Ma, C. F. Leong, D. M. D’Alessandro, H.-Y. Wang, M. Kurmoo, J.-L. Zuo, *Cryst. Growth Des.* **2019**, *19*, 3012–3018.
[31] D. Bechu, G. Rogez, M. W. Hosseini, S. A. Baudron, *New J. Chem.* **2019**, *43*, 14291–14298.
[32] D. Bechu, L. S. Xie, N. L. Breton, S. Choua, M. Dincă, M. W. Hosseini, S. A. Baudron, *Chem. Commun.* **2020**, *56*, 2407–2410.
[33] M. Bendikov, F. Wudl, D. F. Perepichka, *Chem. Rev.* **2004**, *104*, 4891–4946.
[34] N. Avarvari, J. D. Wallis, *J. Mater. Chem.* **2009**, *19*, 4061.
[35] N. Martin, *Chem. Commun.* **2013**, *49*, 7025–7027.
[36] T. Ishiguro, K. Yamaji, G. Saito, *Organic Superconductors*, Heidelberg, Springer-Verlag, **1998**.
[37] H. Kobayashi, A. Kobayashi, T. Nakamura, T. Nogami, Y. Shirota, *Chem. Lett.* **1987**, *16*, 559–562.
[38] T. Nakamura, S. Iwasaka, H. Nakano, K. Inoue, T. Nogami, H. Mikawa, *BCSJ* **1987**, *60*, 365–368.

[39] T. Nogami, K. Inoue, T. Nakamura, S.-I. Iwasaka, H. Nakano, H. Mikawa, *Synth. Met.* **1987**, *19*, 539–544.
[40] J. Garín, R. Andreu, J. Orduna, JoséM. Royo, *Synth. Met.* **2001**, *120*, 749–750.
[41] A. C. Brooks, P. Day, S. I. G. Dias, S. Rabaça, I. C. Santos, R. T. Henriques, J. D. Wallis, M. Almeida, *Eur. J. Inorg. Chem.* **2009**, *2009*, 3084–3093.
[42] B. Schmidt, R. Berger, A. Kelling, U. Schilde, *Chem. Eur. J.* **2011**, *17*, 7032–7040.
[43] N. Svenstrup, J. Becher, *Synthesis* **1995**, *1995*, 215–235.
[44] J.-P. Griffiths, H. Nie, R. James Brown, P. Day, J. D. Wallis, *Org. Biomol. Chem.* **2005**, *3*, 2155–2166.
[45] A. Doménech, H. García, M. T. Doménech-Carbó, F. Llabrés-i-Xamena, *J. Phys. Chem. C* **2007**, *111*, 13701–13711.
[46] T. Yamamoto, M. Uruichi, K. Yamamoto, K. Yakushi, A. Kawamoto, H. Taniguchi, *J. Phys. Chem. B* **2005**, *109*, 15226–15235.
[47] A. Girlando, *J. Phys. Chem. C* **2011**, *115*, 19371–19378.
[48] J.-P. Pouget, P. Alemany, E. Canadell, *Mater. Horiz.* **2018**, *5*, 590–640.
[49] M. H. Whangbo, J. M. Williams, P. C. W. Leung, M. A. Beno, T. J. Emge, H. H. Wang, *Inorg. Chem.* **1985**, *24*, 3500–3502.
[50] G. M. Sheldrick, *Acta Crystallogr. Sect. A* **2008**, *64*, 112–122.
[51] G. M. Sheldrick, *Acta Crystallogr. Sect. A* **2015**, *71*, 3–8.
[52] C. B. Hübschle, G. M. Sheldrick, B. Dittrich, *J. Appl. Cryst.* **2011**, *44*, 1281–1284.
[53] O. V. Dolomanov, L. J. Bourhis, R. J. Gildea, J. a. K. Howard, H. Puschmann, *J. Appl. Cryst.* **2009**, *42*, 339–341.
[54] Gaussian 03 (Revision D.01), M. J. Frisch, G. W. Trucks, H. B. Schlegel, G. E. Scuseria, M. A. Robb, J. R. Cheeseman, J. A. Montgomery, Jr.,T. Vreven, K. N. Kudin, J. C. Burant, J. M. Millam, S. S. Iyengar, J. Tomasi, V. Barone, B. Mennucci, M. Cossi, G. Scalmani, N. Rega, G. A. Petersson, H. Nakatsuji, M. Hada, M. Ehara, K. Toyota, R. Fukuda, J. Hasegawa, M. Ishida, T. Nakajima, Y. Hona, O. Kitao, H. Nakai, M. Klene, X. Li, J. E. Knox, H. P. Hratchian, J. B. Cross, C. Adamo, J. Jaramillo, R. Gomperts, R. E. Stratmann, O. Yazyev, A. J. Austin, R. Cammi, C. Pomelli, J. W. Ochterski, P. Y. Ayala, K. Morokuma, G. A. Voth, P. Salvador, J. J. Dannenberg, V. G. Zakrzewski, S. Dapprich, A. D. Daniels, M. C. Strain, O. Farkas, D. K. Malick, A. D. Rabuck, K. Raghavachari, J. B. Foresman, J. V. Ortiz, Q. Cui, A. G. Baboul, S. Clifford, J. Cioslowski, B. B. Stefanov, G. Liu, A. Liashenko, P. Piskorz, I. Komaromi, R. L. Martin, D. J. Fox, T. Keith, M. A. Al-Laham, C. Y. Peng, A. Nanayakkara, M. Challacombe, P. M. W. Gill, B. Johnson, W. Chen, M. W. Wong, C. Gonzalez, and J. A. Pople, Gaussian, Inc., Wallingford CT, 2004.
[55] A. P. Scott, L. Radom, *J. Phys. Chem.* **1996**, *100*, 16502–16513.
[56] P. Hohenberg, W. Kohn, *Phys. Rev.* **1964**, *136*, B864–B871.
[57] W. Kohn, L. J. Sham, *Phys. Rev.* **1965**, *140*, A1133–A1138.
[58] J. M. Soler, E. Artacho, J. D. Gale, A. García, J. Junquera, P. Ordejón, D. Sánchez-Portal, *J. Phys.: Condens. Matter* **2002**, *14*, 2745–2779.
[59] E. Artacho, E. Anglada, O. Diéguez, J. D. Gale, A. García, J. Junquera, R. M. Martin, P. Ordejón, J. M. Pruneda, D. Sánchez-Portal, J. M. Soler, *J. Phys.: Condens. Matter* **2008**, *20*, 064208.
[60] A. García, N. Papior, A. Akhtar, E. Artacho, V. Blum, E. Bosoni, P. Brandimarte, M. Brandbyge, J. I. Cerdá, F. Corsetti, R. Cuadrado, V. Dikan, J. Ferrer, J. Gale, P. García-Fernández, V. M. García-Suárez, S. García, G. Huhs, S. Illera, R. Korytár, P. Koval, I. Lebedeva, L. Lin, P. López-Tarifa, S. G. Mayo, S. Mohr, P. Ordejón, A. Postnikov, Y. Pouillon, M. Pruneda, R. Robles, D. Sánchez-Portal, J. M. Soler, R. Ullah, V. W. Yu, J. Junquera, *J. Chem. Phys.* **2020**, *152*, 204108.
[61] For more information on the SIESTA code visit: http:// departments.icmab.es/leem/siesta/**.**
[62] J. P. Perdew, K. Burke, M. Ernzerhof, *Phys. Rev. Lett.* **1996**, *77*, 3865–3868.
[63] S. L. Dudarev, G. A. Botton, S. Y. Savrasov, C. J. Humphreys, A. P. Sutton, *Phys. Rev. B* **1998**, *57*, 1505–1509.
[64] Y. Kiyota, I.-R. Jeon, O. Jeannin, M. Beau, T. Kawamoto, P. Alemany, E. Canadell, T. Mori, M. Fourmigué, *Phys. Chem. Chem. Phys.* **2019**, *21*, 22639–22646.

[65] N. Troullier, J. L. Martins, *Phys. Rev. B* **1991**, *43*, 1993–2006.
[66] L. Kleinman, D. M. Bylander, *Phys. Rev. Lett.* **1982**, *48*, 1425–1428.
[67] E. Artacho, D. Sánchez-Portal, P. Ordejón, A. García, J. M. Soler, *Phys. Status Solidi B* **1999**, *215*, 809–817.
[68] H. J. Monkhorst, J. D. Pack, *Phys. Rev. B* **1976**, *13*, 5188–5192.

Table of Content

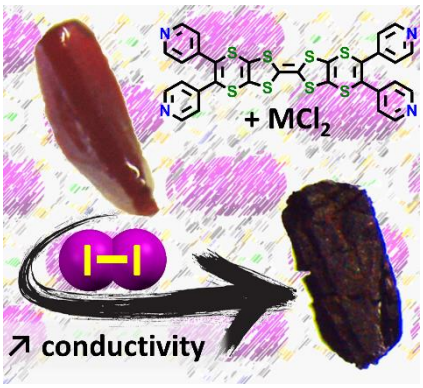

Sulphurous lateral interactions : For electroactive coordination polymers, through space charge transport phenomenon are most often 1D. By increasing the size of the electroactive core, lateral sulphur-sulphur interaction take place and create a 2D conducting pathway. Post-synthetic oxidation is used to increase the materials conductivity.